C h a p t e r   4

Reconstructing the Farallon Plate Subduction beneath North America back to the Late Cretaceous[3]

4.1 Tectonics and Geology Background

Western North America (NAM) has a unique tectonic and geologic history. Since at least Cretaceous time, the westernmost margin of NAM has been a continuous convergent boundary where the Farallon plate subducted and recycled into the mantle. Accompanying the Farallon subduction, terrain accretion and orogeny along the west coast of NAM sustained throughout the Mesozoic and Cenozoic time, with a particularly significant event during the Late Cretaceous to early Tertiary, the Laramide orogeny, reaching as far inland as 1500 km [Burchfiel *et al*., 1992; DeCelles, 2004]. On the other hand, from the middle to the end of the Cretaceous Period, about half area of North America (from the west coast to the middle of the continent) was inundated by shallow seas, forming large thicknesses of marine sediments deposited over a distance of 10^3 km [Bond, 1976; Cross and Pilger, 1978; Liu and

---

[3] This chapter is based on: 1) Liu, L., S. Spasojević & M. Gurnis (2008), *Reconstructing Farallon Plate Subduction Beneath North America back to the Late Cretaceous, Science*, 322, 934–938. 2) Spasojević, S., L. Liu & M. Gurnis (2009), *Adjoint Convection Models of North America Incorporating Tomographic, Plate motion and Stratigraphic Constraints, Geochem., Geophy., Geosys.* 10, Q05W02. **Author contribution:** L. Liu developed the adjoint method and ran all the inverse models; S. Spasojević collected the stratigraphic constraints from literature; M. Gurnis supervised the whole workflow.

Nummedal, 2004; Liu *et al.,* 2005]. Formation of both the Laramide Orogeny and Cretaceous western interior seaway (WIS) has remained enigmatic, and this chapter will focus on the latter.

Earlier studies suggest that the observed Cretaceous flooding of NAM (45% by area) would have required a 310 m sea-level rise, resulting in the accumulation of approximately 700 meters of sediments [Bond, 1976]. Since nearly half of the area of NAM Cretaceous marine sediments is significantly thicker than 700 m, Bond [1976] argued that eustasy could not have been the only process that had operated. Cross and Pilger [1978] attributed the excessive sediment thickness and subsidence to subcrustal loading induced by a shallowly subducted plate. Liu *et al.* [2005] determined that regional subsidence of the western interior consists of a short-wavelength flexural loading component that changed on a time scale of a few million years, and a long-wavelength dynamic subsidence component that changed over a time scale of tens of million years. Liu and Nummedal [2004] determined that the wavelength of a dynamic subsidence component was on the order of 1500 km.

At present, the marine sedimentary rocks with Cretaceous ages lie at an elevation of approximately 1 km, but since the long-term variation of global sea level is less than 300 meters [Miller *et al*., 2005; Haq and Al-Qahtani, 2005], NAM must have subsided and then uplifted over a large length scale. Several numerical models have attempted to explain these inferred vertical motions as dynamic topography induced by negatively buoyant subducting slabs [Mitrovica *et al.*, 1989; Burgess *et al*., 1997; Lithgow-Bertelloni and Gurnis, 1997]. Mitrovica *et al*. [1989] attributed the WIS to shallow subduction of the Farallon plate that could create a ~1,400 km wide region of dynamic subsidence. Specifically, using 2D

isoviscous forward models, subsidence and subsequent uplift was attributed to changes in the dip angle of the Farallon plate. Burgess *et al.* [1997] expanded on this concept with three-dimensional, variable-viscosity models that attempted to match stratigraphic sequence boundaries. These models shared the common attributes of fixing the dynamics to the frame of reference of the overriding (NAM) plate, and fits to the stratigraphic constraints were obtained by changing the subduction depth and dip to obtain best fits to either continental tilt [Mitrovica *et al.*, 1989] or sediment thickness and sequence boundaries [Burgess *et al.*, 1997]. Lithgow-Bertelloni and Gurnis [1997] used a parameterized global mantle flow model with the slabs falling vertically at a constant rate, in which NAM subsided and then uplifted as it moved to the west over the Farallon slab. However, the predicted subsidence and uplift by the models were about 20 Myr earlier compared to the inferred timings [Lithgow-Bertelloni and Gurnis, 1997].

4.2 Data Constraints and Model Setup

In Chapter 3, we designed an iterative scheme that allows the adjoint method to assimilate time-dependent data, e.g. surface dynamic topography, as extra constraints besides present-day mantle structures, which not only recovers the unknown initial condition, but calibrates uncertain mantle dynamic properties that strongly affect mantle convection. For simplicity, this wider-adaptive adjoint scheme only solves for the adjoint of the energy equation rather than those of all three governing equations of mantle (Eqs. 2–4). In this chapter, we apply the adjoint theory to recover the Farallon plate subduction based on actual constraints, including seismic tompography which outlines the present-day mantle structure, plate motions that prescribe the surface velocity boundary condition of the model, and stratigraphy that acts as proxies of surface dynamic topography. The reason for choosing North America is the availability of all the data constraints necessary for the inverse model.

As the starting point of the inversion, the present-day mantle structure, dominated by Farallon subduction, is best represented by seismic tomography. Medium-resolution seismic tomography models obtained by fitting S or P travel time anomalies [Grand *et al.*, 1997; Van der Hilst *et al.*, 1997; Ren *et al.*, 2007; Li *et al.*, 2008] resolve the Farallon slab at mid-mantle depths as a high seismic velocity anomaly beneath eastern NAM. Given the uncertainties in the detailed structure of the slab and differences between S and P wave sensitivities, these models agree moderately well on the spatial distribution, wavelength, and magnitude of the seismic anomaly (Fig. 13). The present-day Farallon slab largely strikes north-south along the U.S. east coast from Central America to the Arctic. In map view, it

has a width of 500–1,000 km while extending from 800 to 2,000 km in depth, with a typical S wave anomaly of about 1%. In this study, we use an updated version of a global shear wave tomography [Grand, 2002]. The reason we didn't use the higher-resolution regional tomography results generated from the ongoing USArray is that these models came out very recently, as is after this part of the research was finished.
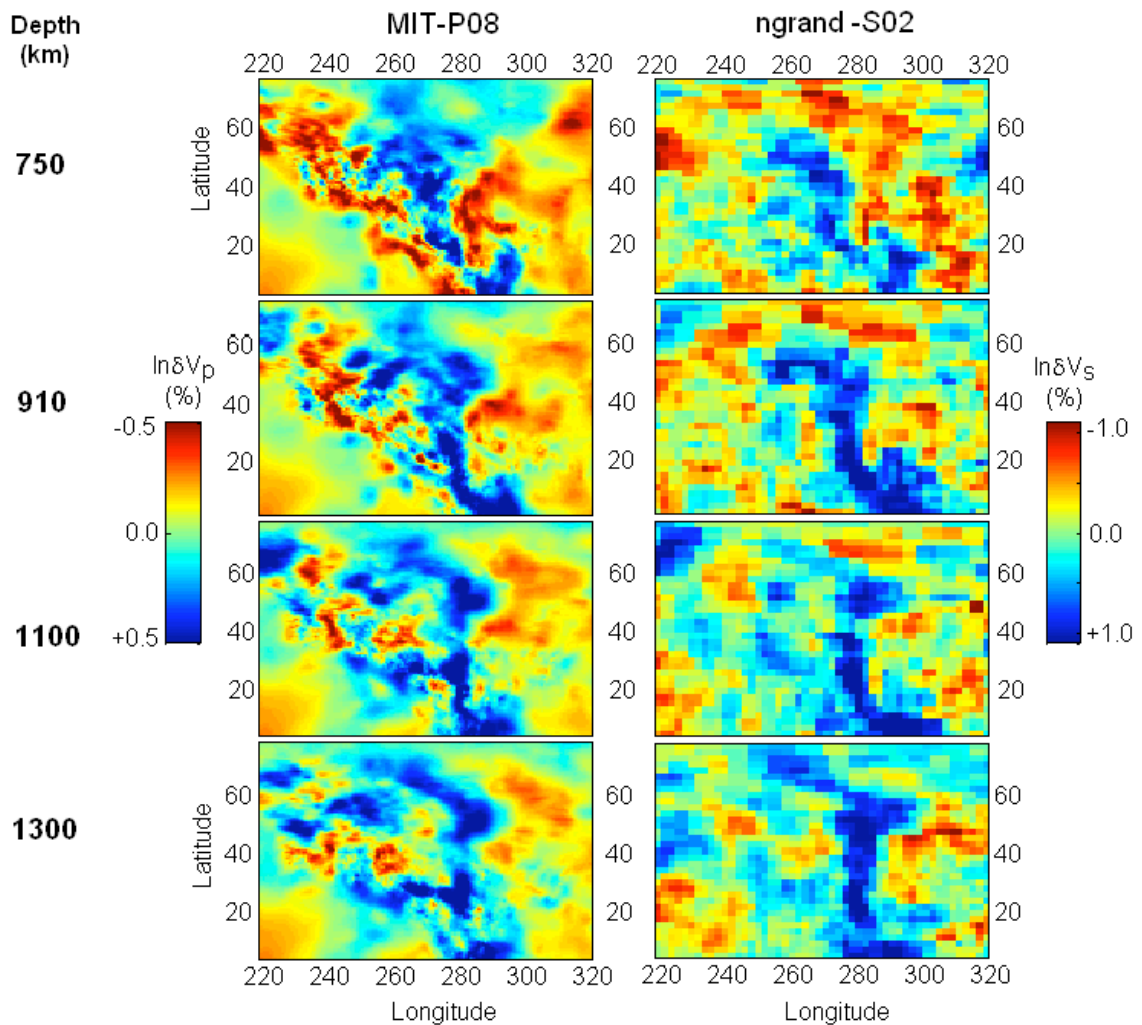
Figure 13 Comparison of the Farallon slab remnants revealed by both a P wave [MIT-P08, from Li *et al.*, 2008] (left) and an S wave tomography [ngrand, from Grand, 2002] (right). Seismic structures are shown at four different depths in the lower mantle under North America, where the Farallon

remnant slabs with largely Late Cretaceous ages are detected. Different color scales are used for the two models. Note the similarity of the two models, especially those of the Farallon remnants (high seismic velocity anomalies).

We use GPlates reconstructions of global plate motions at 1 Ma intervals, in which the plate margins continuously evolve with self-consistent velocities between plates and plate margins [Gurnis *et al.*, 2010]. The rotation of Muller et al. [2008a] is used, implemented in a moving hot-spot reference frame. At 100 Ma, the western margin of NAM is continuously converging from north to south. This persists to 31 Ma, when the Farallon-Pacific ridge intersects the Farallon-NAM trench [Atwater and Stock, 1998], and offshore faults form first followed by formation of the San Andreas Fault in California. The transform segment enlarges at the expense of the convergent margin [Atwater and Stock, 1998] and the Juan de Fuca plate to the north and the Cocos plate to the south continuously shrink. In the south of our region, the Caribbean reconstruction closely follows that of Pindell *et al.* [2006]. From 100 to 80 Ma, North and South America are separated by a spreading center, while the Caribbean region grows by the eastward motion of the Farallon plate between North and South America. At 60 Ma, a new trench and island arc initiates to subsequently become the western margin of southern Mexico and Central America [Pindell *et al.*, 2006].

To constrain the time dependence of the inverse dynamic model, we use paleo shorelines [Smith *et al.*, 1994; Bond, 1978], borehole tectonic subsidence curves [Pang and Nummedal, 1995; Liu *et al.*, 2005] and a set of Late Cretaceous isopachs [Cook and Bally, 1975] associated with the Cretaceous WIS (Fig. 14). The seaway started developing in the

early Cretaceous time by southward transgression from the Arctic and northward transgression from the Gulf of Mexico [Sloss, 1988]. By the Late Cretaceous time the WIS developed into a large epicontinental sea stretching from the Gulf of Mexico to the Arctic, and having an east-west extent of thousands of kilometers [Smith *et al.*, 1994]. Using the boundary between preserved marine and nonmarine sedimentary rocks, Smith *et al.* [1994] defined eight paleoshorelines from Late Cretaceous to present (at 95, 85, 70, 60, 45, 30, 20, 12 Ma). During the Late Cretaceous time, the western edge of the seaway was located close to the Sevier belt [Sloss, 1988; Liu *et al.*, 2005], while the eastern shoreline migrated slightly eastward from 95 Ma to 70 Ma [Smith *et al.*, 1994]. The retreat of the seaway commenced at the end of Late Cretaceous, and the inland sea withdrew completely by the early Cenozoic time [Smith *et al.*, 1994].

After collecting all the data constraints, we assimilate plate motions and seismic tomography in the adjoint convection model to predict stratigraphy, in order to better understand the relation of Farallon plate subduction and vertical motions of the continent. The closed plate polygons describing plate motions allows us to represent the mantle and moving plates with separate reference frames and to better link vertical motions to the stratigraphic record on a plate, as demonstrated for the evolution of Australia [Gurnis *et al.*, 1998].
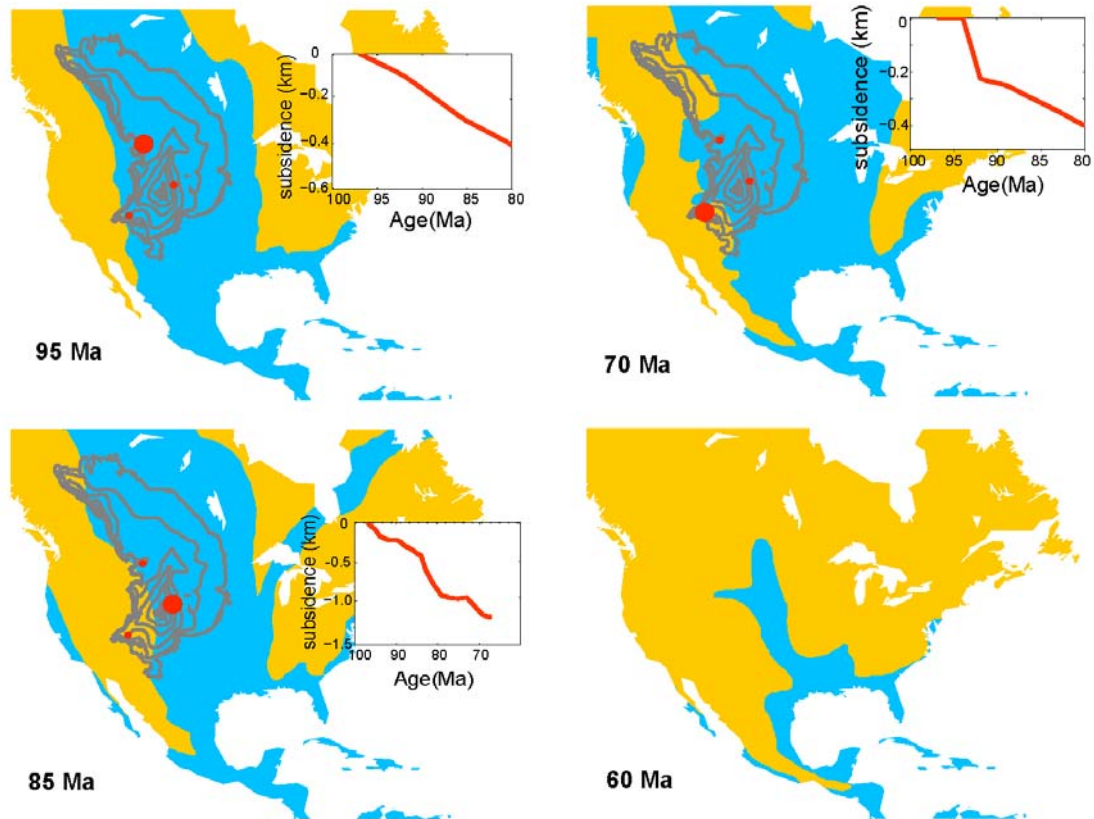
Figure 14 Time-dependent stratigraphic constraints over North America used in the inverse model. Blue areas represent the marine inundations from the Late Cretaceous to early Tertiary. Gray contours show cumulative sediment thickness during the Late Cretaceous. Inset red curves are backstripped tectonic subsidence rates inferred from borehole stratigraphy data, with the corresponding borehole site highlighted with a big red dot (a total of three boreholes are shown). See text for the source of reference.

For simplicity, we model the Farallon subduction by solving equations of a thermal convection system (Eqs. 2–4). This assumption is potentially problematic, as chemical compositions of the subducting oceanic crust and ambient mantle are different. However, since we are looking for a simple representation of the effective density anomalies for both

thermal and chemical structures, we decided to use the term "effective temperature anomaly". Our detailed motivation is as follows. First, below the resolution of the seismic tomography inversion [Grand, 2002], there is a trade-off between seismic anomaly and grid spacing. The absolute seismic velocity anomaly is not uniquely known and the inferred temperature or density cannot be uniquely known. Consequently, our effective temperature anomalies are underestimates of the actual temperature anomalies (assuming that seismic anomalies are thermal in origin, see below). However, because the sinking rate of structures in the mantle and their influence on dynamic topography in the adjoint models are mostly sensitive to net buoyancy, the seismic ambiguity does not adversely influence our inversion scheme. Second, it has now become clear that in addition to thermal effects there is substantial chemical heterogeneity in the mantle [Ni *et al.*, 2002; Ishii and Tromp, 2004; Trampert *et al.*, 2004] and the mapping between seismic anomaly and temperature and density is likely to be both depth- and geography-dependent. In the adjoint models, the dynamic topography and its rate of change are sensitive to density anomalies, which could have both thermal and compositional contributions. However, since the quantity that we are inferring is diffusive, we have decided to refer to it as "effective temperature". Third, both mineral physics and other geodynamic studies suggest that the mapping from seismic shear anomalies to density anomalies do not vary much within the depth range where the present-day Farallon remnants are detected [Karato and Karki, 2001]. Since density variation is what drives mantle flow in our model, this effective temperature is a simple expression of buoyancy while assuming a thermal expansion coefficient that is independent of depth.
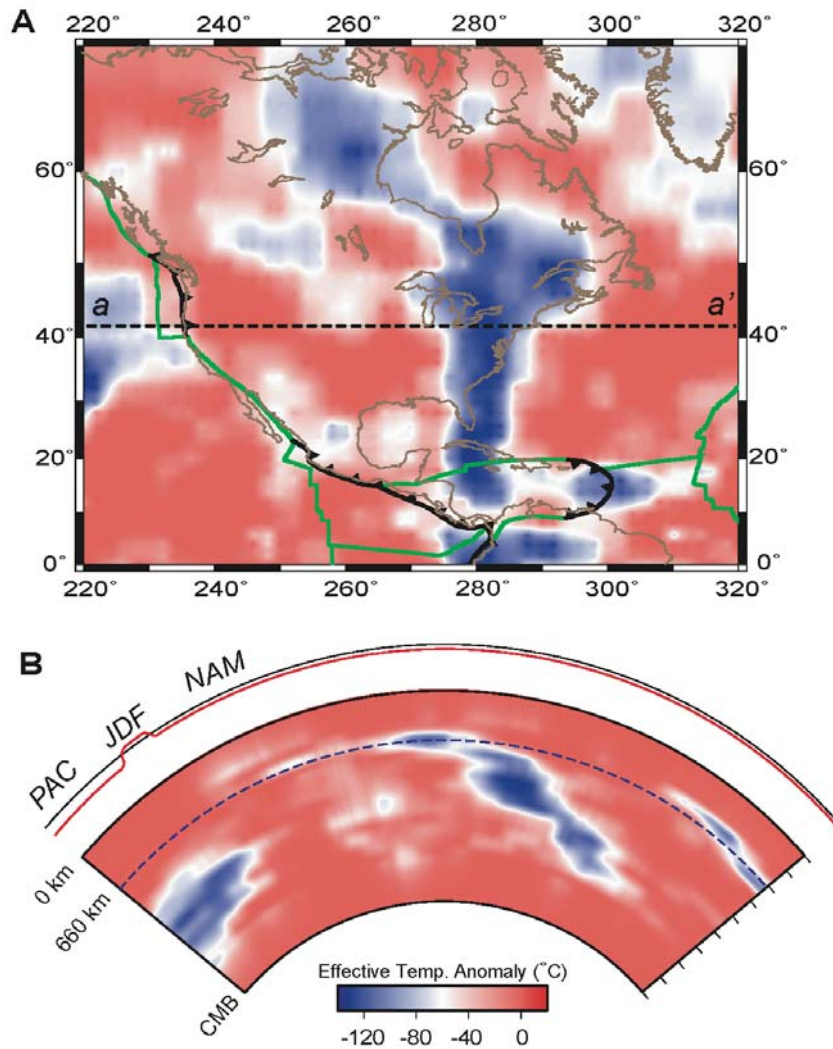
Figure 15 Position and geometry of the present Farallon remnant slabs. A. Map view colors are for 1300 km depth. Green lines represent spreading centers or transform faults, black toothed lines subduction zones, and dark brown lines coastlines. B. Vertical cross-section through the Farallon slabs along 41 °N shown as profile a-a' in A. Red line on top indicates the imposed plate motion, with east being positive. PAC - Pacific. JDF - Juan de Fuca, NAM - North America.

The present-day mantle density (buoyancy) field is first estimated from seismic tomography. The shear wave tomography result from Grand [2002] is converted to effective

temperature anomalies with a scaling factor of 2×10^3 °C/km/s (Fig. 15). The upper 250 km of the seismic signal associated with the North American craton is removed since it is likely neutrally buoyant [e.g., Goes and van der Lee, 2002]. We also remove structures below 2400 km depth where there is a clear gap in the tomographic image. For the rest, we assume a constant seismic to temperature scaling that we will further constrain by fitting the model predictions to stratigraphic data. All values for the physical quantities used in the model are described in Table 3.

Table 3 Parameters for Models with Data Assimilation

Parameter	Symbol	Value
Thickness of the mantle	D	2891 km
Gravitational acceleration	g	9.81 $m\ s^{-2}$
Reference mantle density	ρ_m	3300 $kg\ m^{-3}$
Reference viscosity	η_o	$10^{21}\ Pas$
Thermal diffusivity	K	$10^{-6}\ m^2\ s^{-1}$
Coefficient of thermal expansion	α	3×10^{-5}
Super-adiabatic temperature drop from CMB to surface	T_0	400 $°C$

We first designed a regional model that covers a domain twice as wide (east-west) as the NAM plate, allowing the plate to move since 100 Ma with all observations remaining >1000 km from the vertical boundaries. The reflecting side boundaries caused a lower

mantle return flow restricting the horizontal motion and resulting in the Farallon slab positioned farther to the west in the Late Cretaceous compared to the global model. In order to avoid such artifacts associated with the imposed vertical boundaries, we decide that only global models are suitable for this and similar studies.

Our global model uses 12 caps with 129×129 nodes in each cap (approximately 40 km resolution in map view) and 65 grid points in the radial direction. We assume a free-slip and isothermal core-mantle boundary and an isothermal surface. A Rayleigh number (based on thickness of the mantle) of 9.4×10^6 is used. We parameterize the model with a three-layer viscosity structure, which includes a lithosphere above 100 km with constant 5×10^{22} Pa s viscosity, the upper and lower mantle separated at 670 km depth with varying viscosities to be constrained. We also adopt a temperature dependent rheology, in which laterally viscosity increases exponentially by one order of magnitude for a temperature drop of 200 ℃.

4.3 Constraining Uncertain Mantle Properties

In practice, the inversion for the initial condition given a set of mantle properties is following the algorithm described in Chapter 2, where a first guess based on a simple backward integration is used in order to reduce computational costs. However, constraining of mantle properties including viscosities and slab density anomalies is different from the multi-looping iterative scheme described in Chapter 3, because the actual constraints from the stratigraphic records associated with the WIS allow for a more efficient solution process, as we will detail later.

As discussed earlier, a simple backward integration (SBI) of the present-day mantle temperature anomalies provides a first order estimate for the initial condition of mantle convection. Starting with the 3D structure of Farallon remnant slabs in the lower mantle (Fig. 15), we make an SBI run by reversing the sign of gravity and the sense of plate motions imposed at the surface, so that North America (NAM) moves to the east backward in time and the Farallon slabs move upward toward the surface instead of sinking deeper into the mantle. As can be seen from Figure 16, when the Farallon slab rises into the upper mantle, it deflects eastward rather than westward, and this leads to a geophysically unreasonable subduction geometry where the top part of the slab extrudes far beneath North America instead of connecting to the Farallon plate to the west of the trench. This problem cannot be overcome either by varying the radial viscosity structure or by performing additional forward-adjoint iterations. Such a model is also inconsistent with the temporal sequence of subsidence and uplift of the western interior [Mitrovica *et al*., 1989; Burgess *et al*., 1997]. Essentially, the present Farallon seismic anomaly is too far to the east to be

simply connected to the Farallon-North American boundary in the Mesozoic, a result implicit in forward models [Bunge and Grand, 2000].
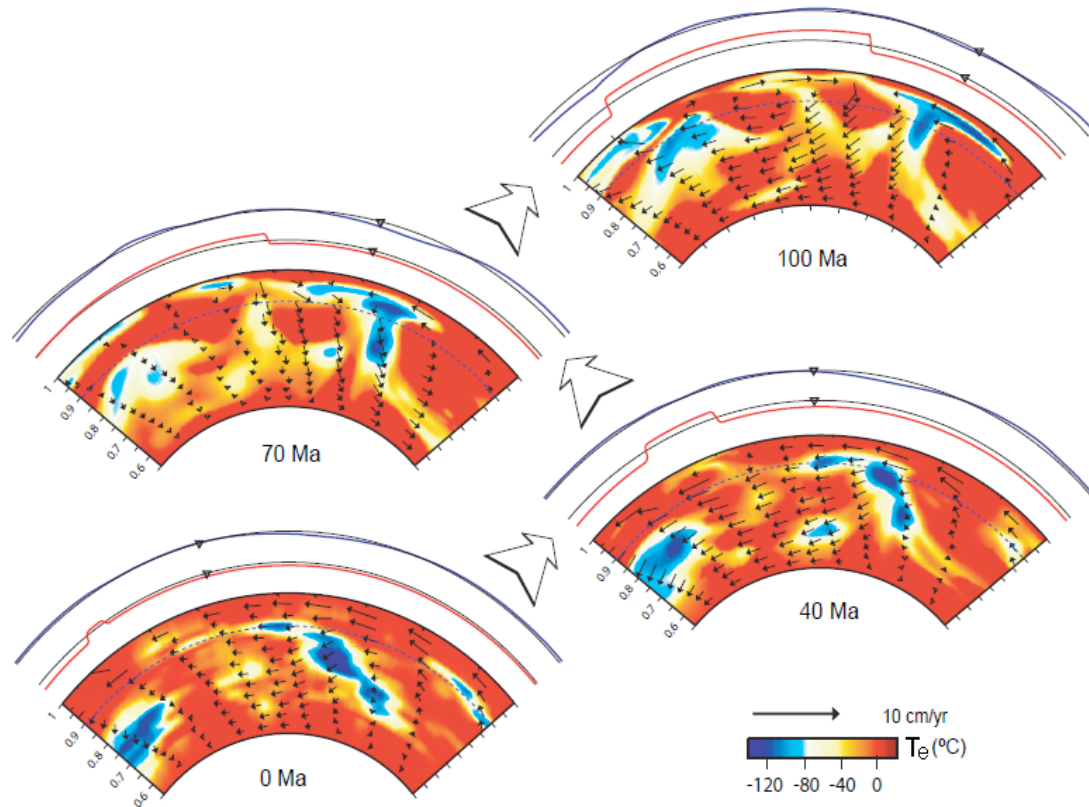
Figure 16 A vertical profile through the whole mantle along 41 °N shows the simple backward integration (SBI) of the Farallon slabs, with the lower:upper mantle viscosity of 15:1 (relative to 10^{21} Pa s) and the maximum effective temperature anomaly (T_e) of 160 °C. Background color represents the temperature field, where the vertical axis shows the normalized radius and the dashed horizontal line represents 660 km depth. Red curves on top show imposed plate motions, and blue curves dynamic topography, with black triangles indicating the position of a borehole site (41.6 °N, 254 °E) about 250 km north of Denver. Arrows indicate the velocity vectors of the mantle flow. Both plate motions and mantle flow are shown in the forward sense of time.

The artifact is inevitable because the present-day Farallon slab does not form a

continuous linear feature in the upper mantle that mechanically connects to the oceanic plate, and therefore, the lower mantle slabs tend to follow the imposed plate motion of North America, rather than that of Farallon. There are two possible causes for this phenomenon. One is that the upper mantle part of the slab has not been detected by seismic tomography due to either poor data coverage or limitation of inversion techniques. Recent higher resolution tomography models still show significant differences in the upper mantle Farallon slab structures [Sigoloch *et al.*, 2008; Burdick *et al.*, 2008; Roth *et al.*, 2008], potentially implying that a robust tomography model of the Farallon slab is yet to come.

Another possible reason is that the Farallon slab indeed broke up during subduction sometime in the past, and this has led to the uncorrelated upper and lower mantle seismic images. Slab failure and breaking is a highly nonlinear dynamic process, whose realization requires sophisticated slab rheology with ultra-high numerical resolution [Burkett and Billen, 2009]. Beside these numerical challenges, there is also little observational evidence that could constrain this possible process. Our global inverse models, with a three-layer mantle viscosity structure and a Newtonian rheology, cannot possibly resolve this detachment process, which would require a more sophisticated forward model with a finer grid.

Since we are only interested in the first order dynamics of the Farallon subduction, we avoid unnecessary complexities by assuming that the oceanic plate should be mechanically coupled to the descending Farallon slab during active subduction. We realize this physical intuition through a stress guide, which consists of a weak horizontal top layer [Manea and Gurnis, 2007] and a high viscosity bottom layer that couples the slab to the

oceanic plate to west of the trench (Fig. 17).
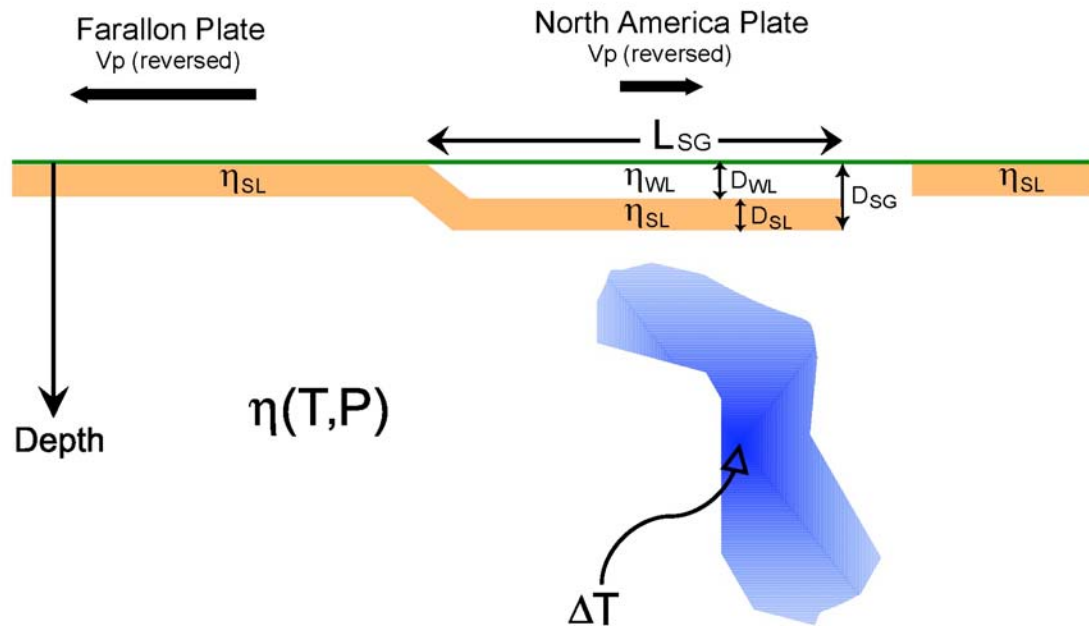
Figure 17 A sketch showing the parameterized stress guide in a trench-normal cross section. The blue structure represents the Farallon slab in the mantle where thermal anomaly drives mantle flow with ΔT being the effective mantle temperature anomaly seen through seismic tomography. The brown-colored layer to the left of the trench represents the oceanic lithosphere and, to the right, the strong layer of the stress guide (at ~100 km depth). Symbol notation: η_{WL} (D_{WL}) is viscosity (thickness) of the weak layer, η_{SL} (D_{SL}) viscosity (thickness) of the strong layer, D_{SG} (e.g. $D_{WL} + D_{SL}$) total thickness of the guide, L_{SG} length of the guide, and $\eta(T, P)$ temperature- and pressure-dependent viscosity.

By incorporating this parameterized stress guide in the inverse model, the cold slab material becomes preferentially attached to the Farallon plate, a process judged more reasonable in terms of actual subduction. Fig.18 depicts the recovered Farallon subduction

after multiple forward-adjoint iterations, with the present-day mantle structure well predicted. Comparison between Fig. 16 and Fig. 18 implies that the stress guide strongly influences slab motion horizontal in the upper mantle, while lower mantle flow is less affected. As the cold slab material rises in a backward sense, the upper part of the slab moves faster horizontally toward the trench than the lower part, and this leads to the formation of a flat to shallow dipping slab around 70 Ma extending 2000 km inland from the trench (Fig. 18).
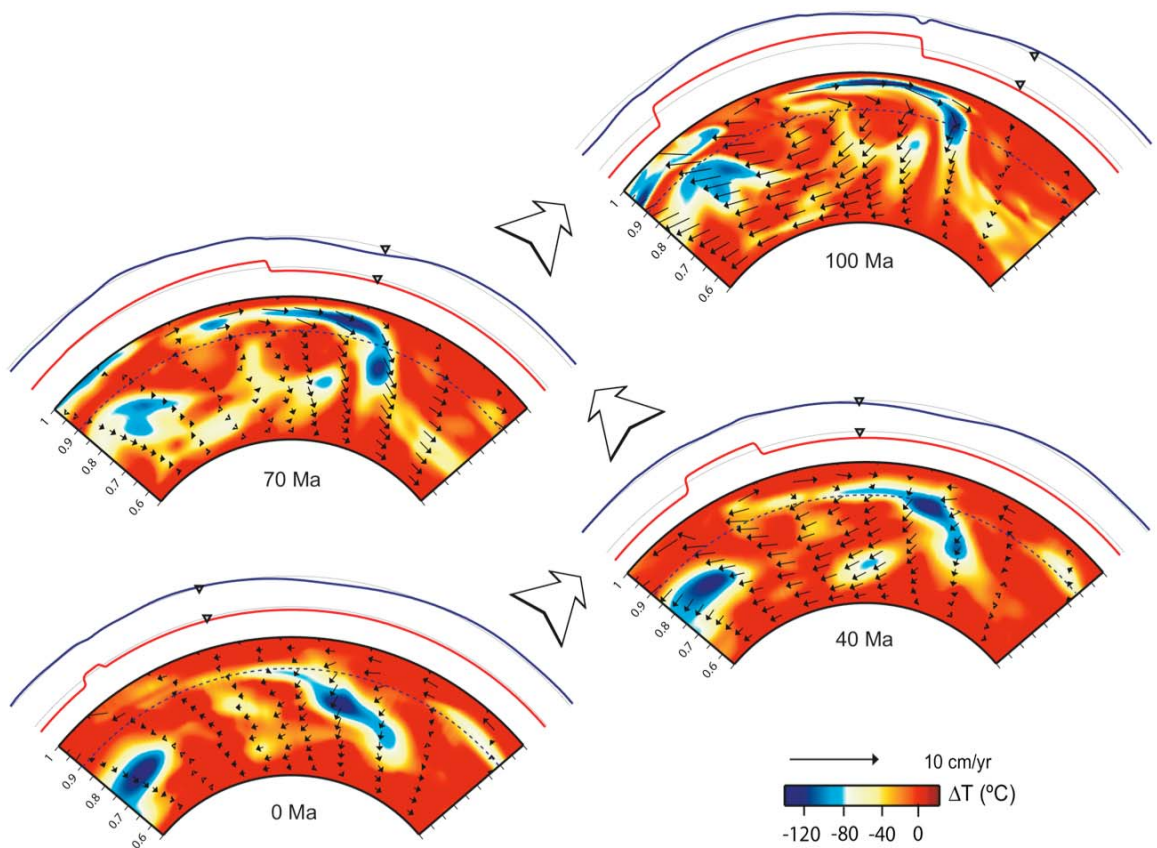
Figure 18 Adjoint recovery of the Farallon subduction, with a parameterized stress guide. Otherwise, the same as Figure 16.

The convergence of the forward-adjoint iterations is shown in Figure 19, for a model with the lower:upper mantle viscosity of 15:1 (relative to 10^{21} Pa s) and the maximum effective temperature anomaly (T_e) of 160 ºC. As the number of forward-adjoint iteration increases (A to C), the structures at 100 Ma become sharper and the predicted mantle structure at 0 Ma converges toward the tomographic image (Fig. 19D). With the increase of iteration number, the residual between the predicted and observed present mantle structure diminishes in magnitude and the initial pattern (A) transforms into a high frequency distribution (C). In addition, the root-mean-squared (RMS) residual with respect to the present day converges after five iterations (Fig. 19E), indicating that the adjoint algorithm is efficient for large scale convection modeling [Chapter 2].
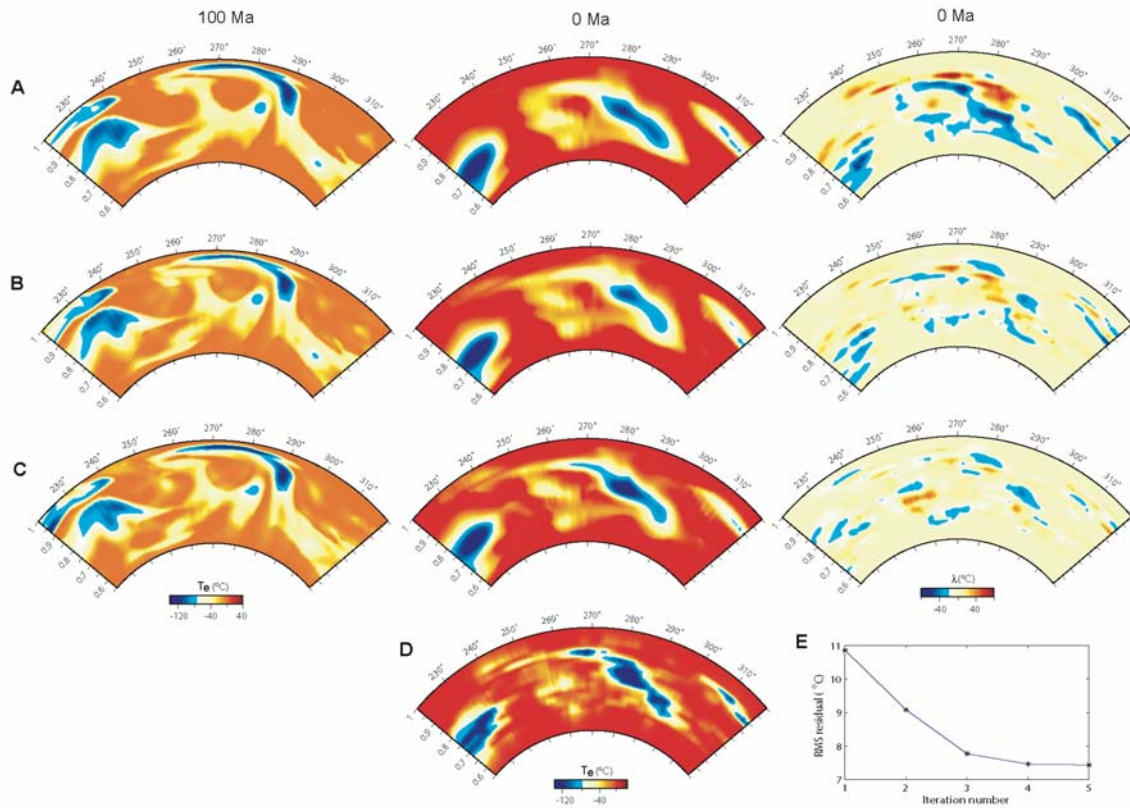
Figure 19 Convergence of the adjoint iterations. A−C corresponds to iteration number 1, 3, and 5, respectively, where the left column indicates initial conditions, the middle final conditions (predictions), and the right residual temperatures. D. Present-day mantle temperature field scaled from seismic tomography. E. Root-mean-squared (RMS) residuals as a function of iteration number.

We examined the influence of the parameterization of the stress guide [Figs. 17, 20B; viscosity of the two layers (η_{SL} and η_{WL}), its thickness (D_{SL} and D_{WL}), and length of the guide under the continent (L_{SG})] on model outcome. For comparison, an SBI run without the stress guide is shown (Fig. 20A). We find that the length of the guide beneath North America must be long enough to capture the Farallon anomaly as it rises into the upper mantle. Stress guides longer than 3000 km lead to similar results (Fig. 20C–E), all similar to Fig. 18. However, if the length is smaller, it fails to recover subduction (i.e., essentially leading to a result like that shown in Fig. 16).

On the other hand, as long as the two layers have a viscosity contrast of more than two orders of magnitude (Fig. 20G–H), we obtain overall results consistent with those shown in the paper. The stress guide leads to the same results when the viscosity contrast is larger, but starts to fail if the contrast is smaller (Fig. 20F). With a total thickness of the stress guide of 130 km ($=D_{WL}+D_{SL}$), the shape of the recovered slab is not sensitive to the relative thickness of the two layers inside the guide. Furthermore, we can show that the imposed plate motion and the stress guide neither increase nor decrease the vertical velocities in models with plate motions (Fig. 20A) or with both plate motions and the stress guide (Fig. 20J), compared to those without imposed plate motions (Fig. 20K). Overall, the result of subduction beneath North America is robust in that it can be reached with a wide

range of stress guide parameters and that the relevant dynamics and geophysical implications remain unchanged.
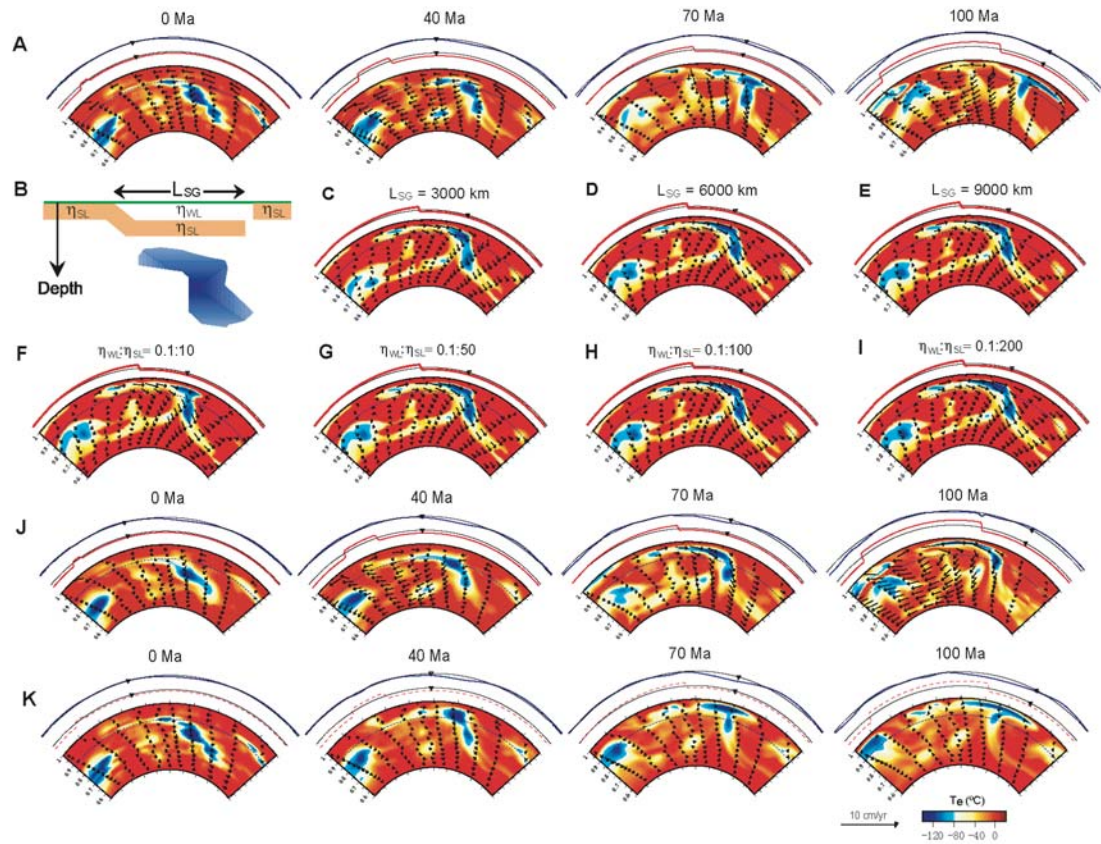
Figure 20 Subduction modeling with inverse method. All cross sections are at 41 °N, with the velocity vectors (black arrows) plotted over the temperature field (in color). Dynamic topography (blue) and plate motions (red) along the profile are shown above the cross-section. The black triangle denotes a borehole site (41.6 °N, 254 °E) that moves with the continent. All runs have a lower mantle viscosity $h_{LM} = 15$, $h_{UM} = 1$ and an effective temperature anomaly Te = 160 °C. (A) An SBI run with a standard model from present-day mantle structure leads to unrealistic subduction geometry back in time, indicating the requirement of a stress guide. (B) A sketch of the parameterized stress guide showing an imposed small viscosity (h_{WL}) layer overlying a large viscosity (h_{SL}) layer underneath the continent, where LSG indicates the length of the guide. The

recovered slab at 70 Ma (C−E) with the different values of L_{SG} and (F−I) with various viscosity ratios (relative to 10^{21} Pa s) within the two layers, showing the solutions converge as long as $L_{SG} >$ 3000 km and h_{WL}: $h_{WL} < 0.1$:50. (J) The evolution of the slab after five forward-adjoint iterations including a stress guide with LSG = 6,000 km and h_{WL}: h_{WL} = 0.1:100, where reasonable subduction geometry develops. (K) A free convection test showing that without the imposed plate motions and stress guide, the slab has almost the same vertical velocities as can be seen from the depth of the structure at different times.

By inverting the Farallon slab subduction, we can also predict the dynamic topography on the surface as a function of time, which can constrain the uncertain mantle dynamic properties. In Chapter 3, we show how to constrain mantle properties by fitting the evolving dynamic topography recorded at one single site on the surface. In practice, we find that there are substantial constraints on the stratigraphy of WIS, including multiple boreholes with backstripped tectonic subsidence rates, several reconstructed paleo-shorelines marking the extents of the continental flooding at different geological times, and an isopach map showing the spatial variation of Cretaceous marine sediment thicknesses (Fig. 14). The extra power of constraints helps to reduce the amount of work involved in constraining mantle properties compare to the synthetic experiments in Chapter 3, as we demonstrate in the following subsections.

4.3.1 Effective Slab Temperature Anomaly

We attempt to put constraints on three model variables: upper mantle viscosity η_{UM}, lower mantle viscosity η_{LM}, and the effective temperature anomalies T_e scaled from seismic shear velocity perturbations.

Using a range of values for the effective temperature anomalies, we find that the recovered slabs have nearly identical geometries if the lower mantle viscosity is compensated so that the Rayleigh number remains invariant. In these cases, the convective velocities are nearly the same, except for small differences in the lateral variations in viscosity associated with temperature, so that the evolution of slabs remains the same for all cases (Fig. 21). Correspondingly, the predicted flooding has the same positions following the slab geometry and provides an opportunity for comparing the effects of different effective temperature anomalies on flooding.
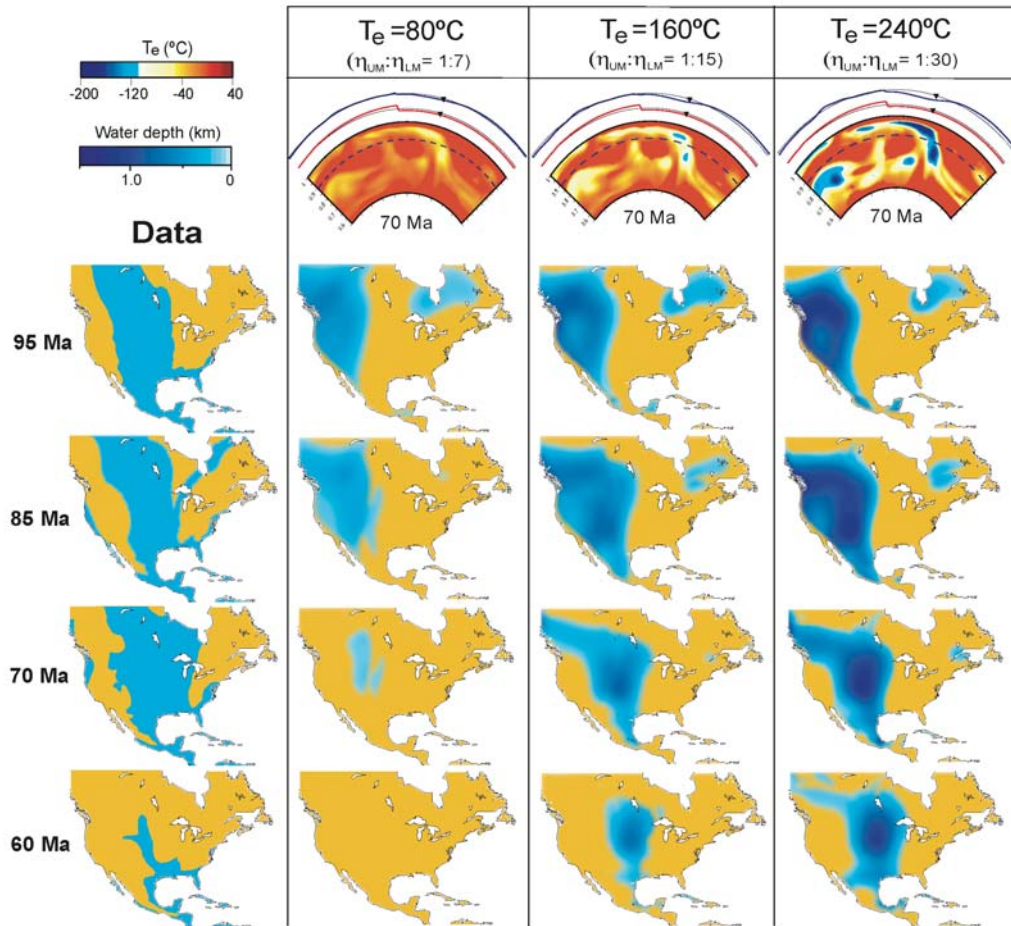
Figure 21 Constraining the effective temperature through flooding predictions. The left (column

1) shows the extents of Western Interior Seaway (WIS) from Late Cretaceous to early Tertiary, as reconstructed by Smith *et al*. [1994]. The right (columns 2−4) list the predicted WIS from three inverse models. These three models have different magnitudes of temperature anomaly (80, 160, and 240 °C, respectively) and lower mantle viscosities largely traded off with temperature ($7{\times}10^{21}$, $15{\times}10^{21}$, and $30{\times}10^{21}$ Pa s, respectively; all cases have an upper mantle viscosity of 10^{21} Pa s), where all three models produce the same slab geometries (the 70 Ma slab shown on top). The model with the 160 °C temperature anomaly matches observations the best.

On the other hand, although the dynamic topography has the same spatial pattern for cases with different effective temperature anomalies, the magnitudes of dynamic topography differ (Fig. 21). The extent of predicted flooding also varies depending on dynamic subsidence: With an effective temperature anomaly of 80 °C, the flooding occurs widely over the west at 95 Ma, but disappears soon after (Fig. 21); with a larger anomaly (240 °C), the flooding is well correlated with WIS, but persists after the Cretaceous; the flooding is well predicted with an anomaly of 160 °C in both time and space. This value of effective temperature anomaly will be used in subsequent models.

4.3.2 Lower Mantle Viscosity

For a given density, the timing and extent of the flat slab formation depend on mantle viscosity, especially lower mantle viscosity, because the slab has a longer path in the lower compared to the upper mantle. From experiments, we find that the upper mantle viscosity has a minor role in controlling the overall pattern of the WIS predictions. The surface dynamic topography associated with the descending slab causes the continent to

subside dynamically and results in marine deposition, if below sea level. In practice, we assume that the sedimentation rate was constant and we impose a eustatic curve while isostatically adjusting basin depth after each time step of 1 Myr. Therefore, the observed extent of Cretaceous flooding (Fig. 14), besides constraining slab density (i.e., T_e), also provides direct constraint on lower mantle viscosity for a fixed density anomaly. Fig. 22 demonstrates this process.
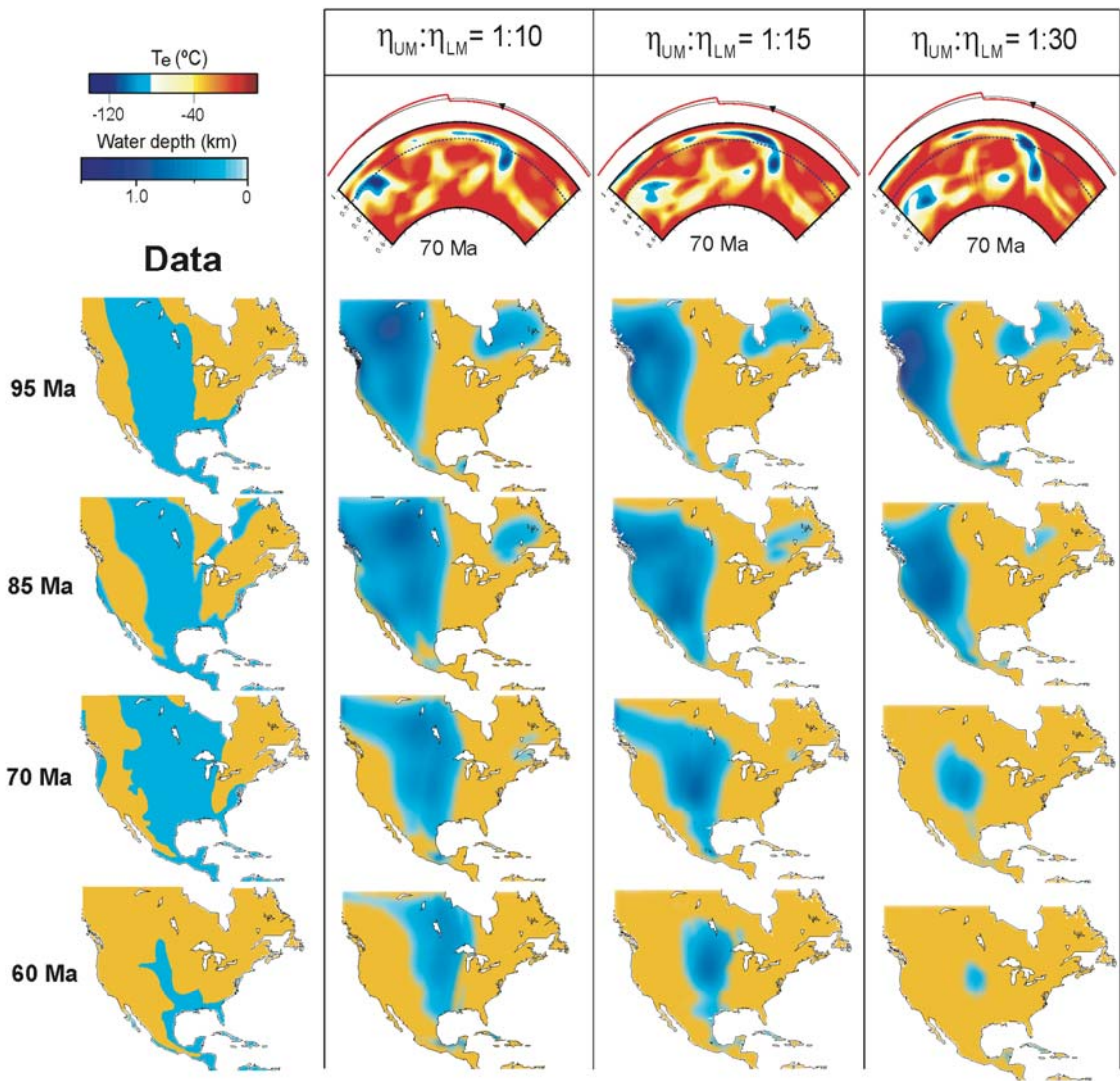
Figure 22 Constraining lower mantle viscosity through predicting the position and extent of WIS,

given a density anomaly. Column 1 shows the reconstructed WIS. Columns 2–4 show predicted flooding from three models with different lower mantle viscosities (10×10^{21}, 15×10^{21}, 30×10^{21} Pa s, respectively; T_e is the same as inferred from Figure 21).

As seen in Fig. 22, in a backward sense, a high viscosity (3×10^{22} Pa s) lower mantle causes the slab to rise slowly, reach the surface closer to the trench, and form a small area of flat slab subduction; the associated dynamic subsidence causes flooding with a smaller wavelength over shorter duration than observed (Fig. 22, column 4). Alternatively, a mantle of smaller viscosity causes the slab to rise faster and reach the surface farther from the trench, while forming a larger area of flat slab subduction, which causes extensive flooding spatially and temporally (Fig. 22, column 2). A good fit to observed flooding is obtained if we decrease the lower mantle viscosity to 1.5×10^{22} Pa s (Fig. 22, column 3).

Another viable means to retrieve lower mantle viscosity is to predict dynamic topography and its rate of change by comparing the fit to borehole tectonic subsidence curves and their temporal variation. For more details about this approach, please refer to Spasojevic *et al.* [2009].

4.3.3 Upper Mantle Viscosity

The rate of change of dynamic topography is inversely proportional to the upper mantle viscosity (Chapter 3). If we consider the vertical motions evident in WIS as proxy of absolute dynamic topography, and the backstripped tectonic borehole subsidence curves as rates of change of dynamic topography, we can infer the value of upper mantle viscosity by fitting the borehole subsidence rates as shown in Fig. 14.

There are 12 boreholes used in total, sampling the Cretaceous isopachs along east-west and north-south sections, which provide constraints on the upper mantle viscosity (Fig. 23A). If the upper mantle viscosity is too small, the slab sinks too fast, and the resulting subsidence rate is too large; as the upper mantle viscosity increases, the corresponding rate of change of subsidence decreases, and by best fitting these subsidence curves, we conclude that the upper mantle viscosity is about 1×10^{21} Pa s (Fig. 23B shows three such boreholes). On the other hand, a root-mean-squared (RMS) measure of the misfit from all boreholes may provide additional constraints. Fig. 23C plots these misfits along both the EW and NS lines, with the borehole listed as a function of distance from the west (north) end. Systematically, the misfits for the case with upper mantle viscosity of 1×10^{21} Pa s are the smallest among all experiments, validating the result from comparing the rates (Fig. 23B).
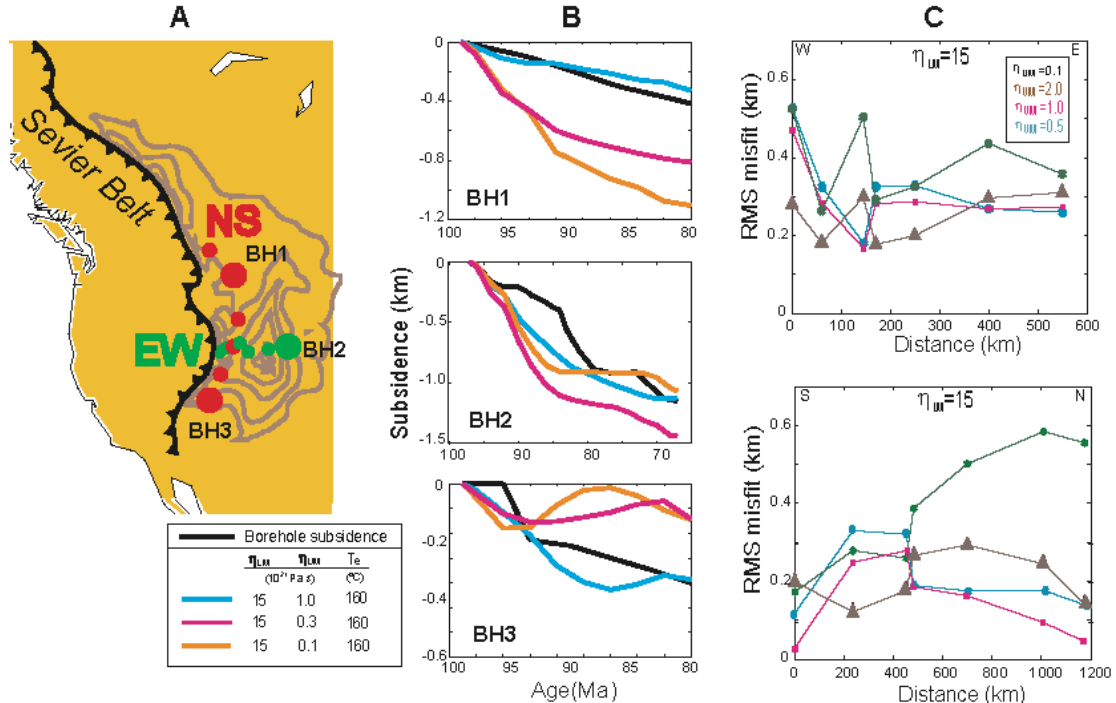
Figure 23 Constraining upper mantle viscosity with subsidence rates and RMS misfits. A. Site

locations of all boreholes (color dots) sampling the Cretaceous sediment isopach (brown contours), where three representative boreholes (big dots, i.e., BH1−3) are chosen to show the predicted subsidence rates. B. Observed (black) and predicted (color) dynamic subsidence rates at three borehole sites shown in A. Model parameters for these experiments are shown at the bottom of panel A. C. RMS misfits for all boreholes (triangles) along both the EW and NS sections.

We conclude this section by showing more models with different upper and lower mantle viscosities, in order to expand the parameter space explored (Fig. 24). As seen, the one with upper/lower mantle viscosity ratio of 1/15 is the best-fit model (Fig. 24B).
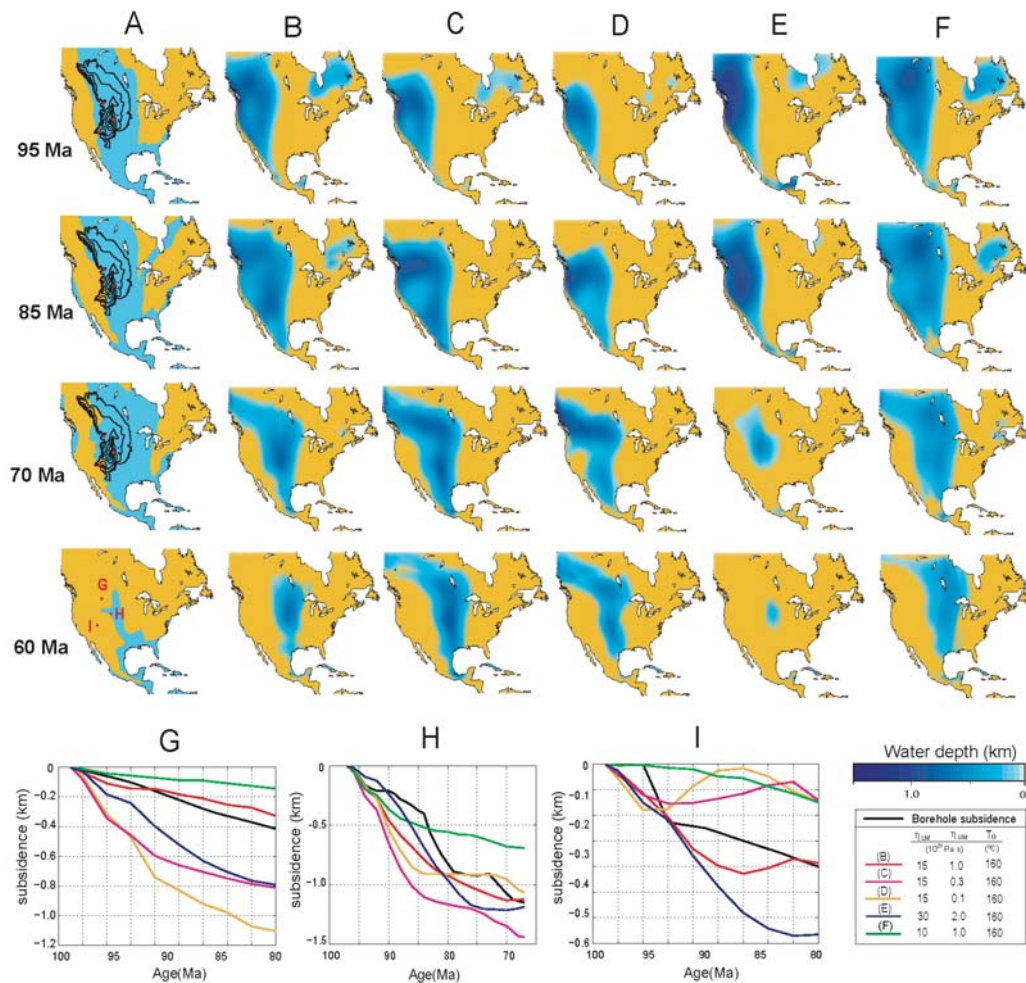
Figure 24 More models showing the effects of mantle viscosities on flooding predictions and borehole subsidence. (A) Observed flooding [Smith *et al*., 1994]. (B−F) Predicted flooding with different models (parameters are given in the bottom right corner; viscosities relative to 10^{21} Pa s). (G−I) Borehole subsidence predictions (colored lines) compared to observations (black line).

4.3.4 Discussion

We attempted to constrain the uncertain mantle dynamic properties, including upper and lower mantle viscosities, and effective temperature anomalies associated with the subducting oceanic slabs. Our inferred mantle viscosities fall in the range of published values, including estimates from studies of postglacial rebound [Mitrovica and Forte, 1997; Milne *et al*., 2004; Paulson *et al*., 2007] and modeling the geoid [Richard and Hager, 1984; Hager, 1984] for the region of North America. The range of published values for the upper mantle viscosity (averaged if multiple layers were parameterized) is ~0.5-1×10^{21} Pa s, and that for the lower mantle is ~2-30×10^{21} Pa s. The upper/lower mantle viscosity ratio of 1:15 we infer falls within the middle of the earlier published values.

Conversion of a seismic-velocity anomaly recovered from tomography into a mantle density anomaly can be defined as a density/velocity ratio

$$R_{\rho/S} = \frac{\Delta\rho/\rho_0}{\Delta V_S/V_S} \tag{23}$$

where $\Delta\rho/\rho_0$ is the density perturbation, and $\Delta V_S/V_S$ is the shear wave velocity anomaly.

Earlier studies predicting geoid [Forte *et al*., 1994; Cadek and Fleitout, 1999] or plate

motions [Simons *et al.*, 2007] suggest that this ratio ranges from 0.1 to 0.35. Our preferred density anomaly associated with the Farallon remnant slabs indicates a value of 0.35, at the top end of previous inferences. Our inference by fitting surface stratigraphy, however, is not directly comparable with other studies, because this ratio is constrained when the Farallon slab was at a much shallower depth than its present-day position, where the compressibility of mantle materials reduces this ratio as the slab sinks deeper. Given a density reduction factor of 2 from the flat slab stage during Late Cretaceous to its current mantle depth (~1400 km), the implied density/velocity ratio of ~0.2 is well within the range inferred by other studies.

Our inferred mantle properties are subject to change, and there are several reasons. First, the three-layer mantle viscosity structure is probably too simple to represent the earth, and the viscosity change from the upper to lower mantle may be gradual. But we are not confident that the current data assimilated in the inverse model can constrain a more sophisticated mantle rheology. Second, we assume a spatially uniform scaling from seismic velocity anomaly into density and this assumption may not be exact, as the response of different minerals to seismic properties and density varies. Existence of chemical heterogeneity inside the slab, for example an oceanic plateau, tends to respond differently to seismic wave speeds from the ambient slab. Third, as the resolving power of seismic tomography increases, the mantle image will evolve, which will certainly change the circulation pattern associated with these structures. Finally, omission of phase changes, both along the major seismic discontinuities and a possible basalt to eclogite transformation within the crust of the oceanic plate upon subduction, may trade off with the inferred

dynamic parameters of mantle. Specifically, phase changes at 410 and 660 km depths may increase and decrease, respectively, the velocity of the sinking slabs and, in some cases, trap slabs within the transition zone [e.g., Christensen, 1996; Cízkova *et al.* 2002]. Neglecting the phase transitions could have led to an overestimate of slab velocity, which in turn requires a larger lower mantle viscosity to counteract the buoyancy. This trade off, however, is likely to be a secondary effect, because the density anomalies associated with these phase transformations are minor compared to the total buoyancy of slabs, and the two phase changes have opposite Clapeyron slopes that will canceling each other if the subducting slab is strong enough [Billen, 2008]. The omission of the phase change of the crust by assuming a uniform density within the slabs, however, may affect the inferred temperature scaling from seismic velocity anomalies, especially in the presence of a possible oceanic plateau, as we will discuss more in the next chapter.

Another aspect of the inverse model that needs further improvement is to use more realistic rheology structure to replace the stress guide. In effect, the stress guide represents an enhanced version of temperature-dependent viscosity, plus a weakly coupled interface between the down-going slab and the overriding plate. With a better seismic image of the upper mantle structure beneath the western U.S., in which the younger part of the Farallon slab is better resolved and will presumably form a continuous subduction system, the stress guide may then be replaced by a strong slab with temperature-dependent viscosities. In this case, the continuity of the seismic image will provide a sustained mechanical coupling between the surface oceanic plate and the down-going slabs inside the mantle during active subduction.

On the other hand, the inverse model can be further validated by comparing with more independent observations, as will be one of the main themes of Chapter 5. With these new constraints, we can show that the inverse model we have developed fits a variety of observations, supporting its physical validity.

4.4 Flat Subduction of Farallon Plate during the Late Cretaceous

By predicting the formation of the Western Interior Seaway (WIS), while providing constraints on mantle dynamic properties, we recover the Farallon plate subduction back to the Late Cretaceous. Formation of this continental marine inundation is due to broad scale surface dynamic subsidence induced by the dense down-going oceanic slabs beneath North America (Figs. 21, 22, 24).

From structural geology and the history of magmatism [Coney and Reynolds, 1977; Henderson *et al.*, 1984; Saleeby, 2003], it has long been postulated that a flat slab of the subducting Farallon plate lay beneath the western United States during the Late Cretaceous to early Cenozoic. This flat slab is thought to have occurred within a restricted area covering several states including Wyoming, Utah, Colorado, Arizona, and New Mexico. Our inverse models, by explicitly bringing the old Farallon remnant slabs back to the position where they subducted, provide complementary evidence for this flat-subduction episode.

At 100 Ma, the slab is shallow dipping, but not flat lying (Fig. 25A). Slab flattening starts at about 90 Ma progressively from the trench, and is characterized by a patch of thickened oceanic lithosphere about 1000 km wide, which subducts to the northeast (Fig. 25B). The model predicts that this segment of the Farallon slab evolved into an isolated and thickened patch of oceanic lithosphere bounded by a series of shallow to steep dipping fragments (Fig. 25D). This configuration is sustained throughout the Late Cretaceous, accompanying a vast inland migration of the whole slab. In the model, the flat lying slab sinks vertically from 70 Ma (Fig. 19). The inferred position of flat lying subduction from the adjoint model correlates with the region of basement cutting Laramide-type faults in the

western U.S. from 80 to 65 Ma [Saleeby, 2003]. Our best model matches the along–strike extent of the faulting and its maximum inboard extent (Fig. 25B–D). However, both the onset and demise of flat subduction occur 10 Myr earlier in the model compared to the structural and magmatic constraints. We made no attempt to tune model parameters based on the geologically inferred position of flat subduction.
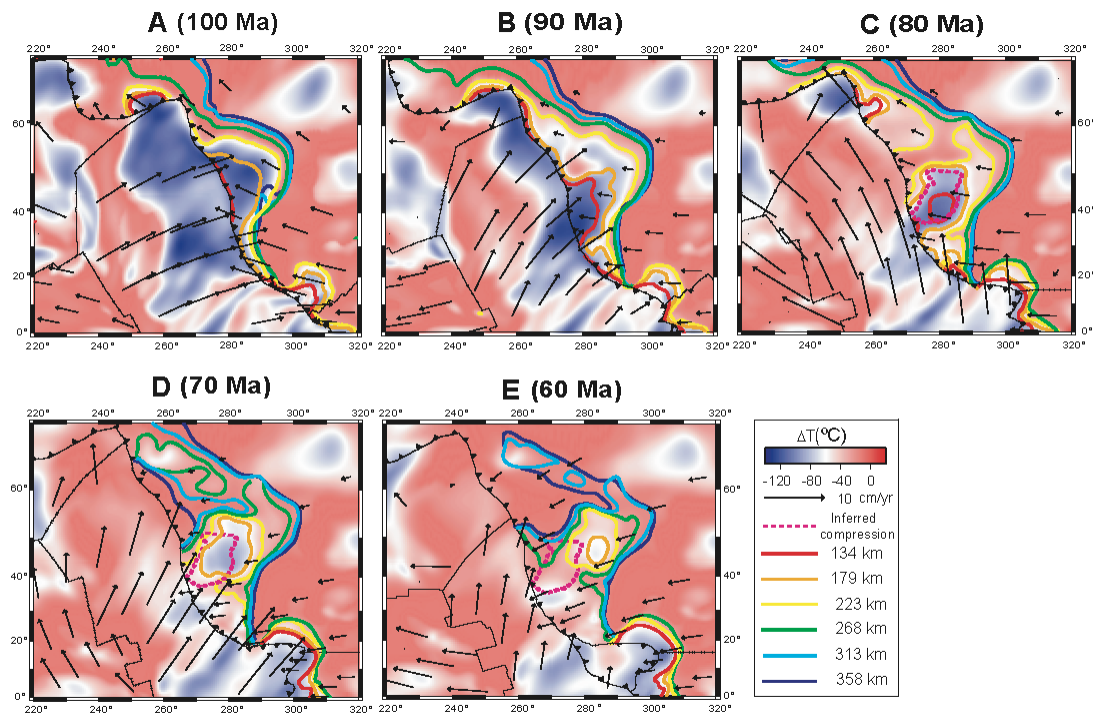
Figure 25 Map view of evolution of the Farallon subduction from the Late Cretaceous (A–D) to the Early Tertiary (E). The background temperature is at depth 223 km and velocity vectors indicate imposed plate motions. The color lines (isotherms for temperature 30 ℃ lower than ambient mantle) indicate the upper boundary of the slab at different depths with a warm (cold) color representing a small (large) depth. The dashed pink contour outlines the geologically inferred surface compression area occurring between 80 and 65 Ma [Saleeby, 2003].

We want to point out that depths of these slab contours (isotherms in Fig. 25) make more sense in demonstrating the relative position of different parts of the slab than representing their absolute depths. Because the global model has a radial grid resolution of about 45 km, the inferred absolute depth of slabs is poorly resolved. In fact, these slabs seem to be too deep (almost all below 100 km), in terms of explaining the corresponding surface geology that may require shallower slab underplating, say, at ~50 km (more discussion in Chapter 5.2). Future models with higher numerical resolutions should consider producing more realistic radial positions of the flat slab.

By projecting the Farallon flat slab into the reference frame of North America, we can obtain a clearer picture for comparison between the flat slab evolution (Fig. 26) and various geological observations. On top of the slab contours, we plot the Colorado Plateau, a distinct geological unit that survived most of the tectonic deformations during Mesozoic and Cenozoic time [Burchfiel *et al*., 1992], and the geologically inferred Laramide province [Saleeby, 2003]. We also find that the rapid destruction and exhumation of the southernmost Sierra Nevada batholith [Saleeby *et al*., 2007] correlates with the passage of the flat slab in Southern California, both spatially and temporally.

Besides identifying the geologically inferred flat slab, we further find that this flat slab is not an isolated piece of oceanic plate, but rather that it is a thicker and shallower portion of a continuous slab that extends from Western Canada to Mexico (Fig. 25). The adjoint models suggest that a vast zone of shallow dipping subduction extended more than 1000 km eastward and northward from the zone of flat lying subduction, especially from 90 to 70 Ma (Fig. 25B–D). The zone is larger than inferred from a simplified set of forward

models that neither incorporated the details of subduction nor attempted to match stratigraphy [Bunge and Grand, 2000].
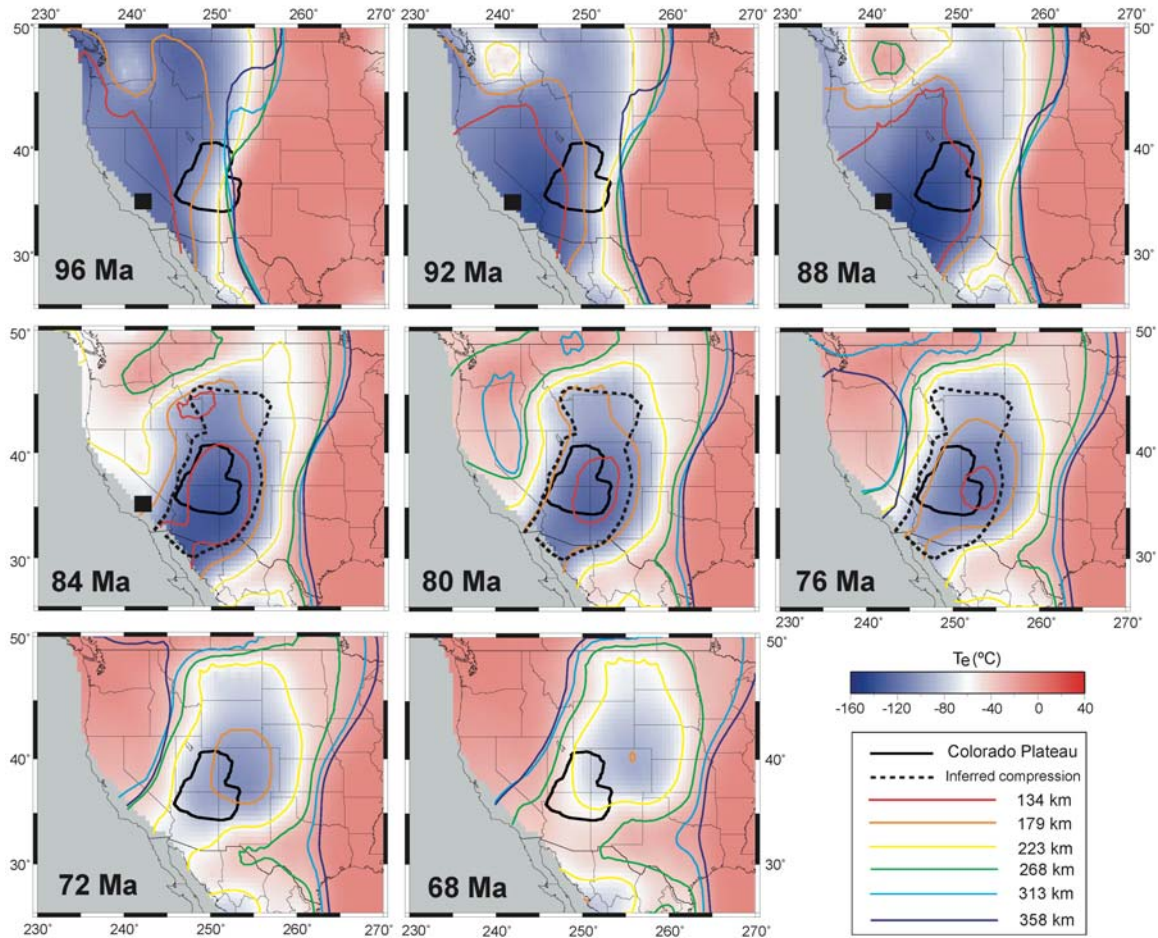
Figure 26 Three-dimensional delineation of the recovered Farallon slab during the Late Cretaceous from our preferred model in the reference frame of fixed North America: color contours depict an isotherm at various depths (these isotherms are 40°C lower than the ambient mantle that represent the edge of the Farallon slab at these depths); the background temperature field is shown for 223 km depth. All time snapshots are projected onto the North American plate. The black square in Southern California represents the location of southernmost Sierra Nevada batholiths during the exhumation event described by Saleeby *et al.* [2007]. The black dashed contour outlines the geologically inferred

Laramide compression zone [Saleeby, 2003].
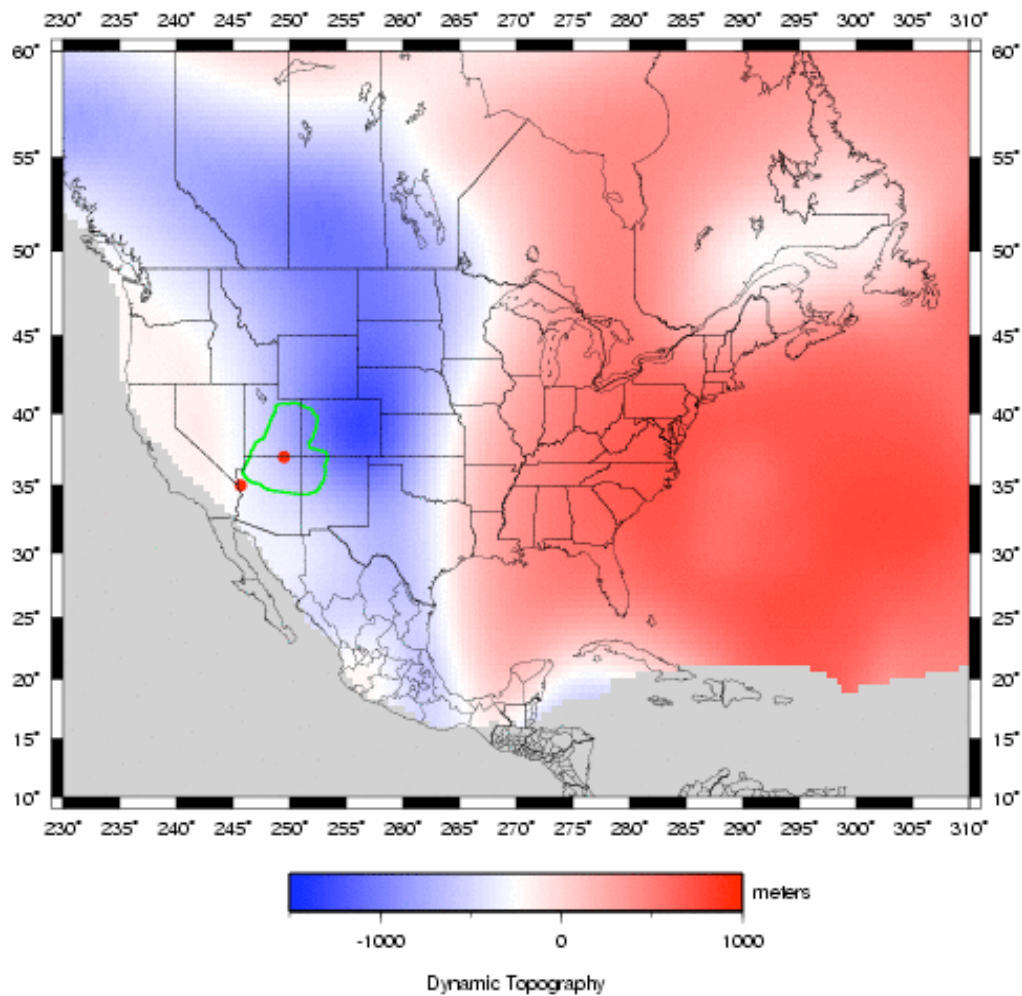
Figure 27 Predicted dynamic topography over North America at 70 Ma. Green contour represents the Colorado Plateau, and the two red dots span a profile along which Flowers *et al.* [2008] inferred for independent constraints for the topography evolution of the Colorado Plateau (more discussion in Chapter 5).

The broad shallow to flat subduction beneath North America caused surface subsidence across the entire western North America (Fig. 27). Therefore, the region of

dynamic subsidence for North America, previously thought to be confined to portions of the western U.S. [Mitrovica *et al.*, 1989; Burgess *et al.*, 1997], was likely substantially larger in extent and mostly characterized by a Cenozoic unconformity [Burgess *et al.*, 1997]. Much of the Canadian shield is sediment free, and the region has not been used to constrain dynamic models, but our model predicts this area also subsided during the Late Cretaceous, consistent with a recent low temperature thermochronology study for basement samples in western Canada indicating a history of sediment burial and unroofing occurred during the Cretaceous-Cenozoic time [Ault *et al.*, 2009]. This suggests that there is substantial ability to infer tectonic events when an adjoint of the convection problem is applied to seismic and plate motion data.

Upon inverting the Farallon subduction as described above, an immediate question to ask is what caused the flat subduction localized along the western U.S. during the Late Cretaceous? The adjoint inversion technique itself cannot be the answer. This is because the present-day seismic image, the starting point of the adjoint inversion, already has a "dome"-shaped structure in it located below the Great Lakes region (Fig. 28). This dome, when advected back to the surface, ultimately leads to the flat slab configuration (Fig. 25).

Specifically, we can track the three-dimensional evolution of the mantle structures in the inverse model (Figure 29). At present day, there is a prominent east-west anomaly (facing east; Figure 29I) occurring at ~1700 km depth, and another broader and obliquely dipping north-south anomaly (facing northwest; Figure 29E) at ~1400 km (cross sections of these structures show their dimensions). These two prominent anomalies form the hook structure well described in the literature [Ren *et al.*, 2007], while inside the 'elbow' is a dome shaped structure with its 'roof' going up toward the west. As these structures are

reversed backward in time (Figure 29B–D, F–H), the dome structure evolves into the flat lying patch of the Farallon slab while the hook structure evolves into the shallow dipping halo (from 100 Ma to 70 Ma) described in Figures 25, 26.
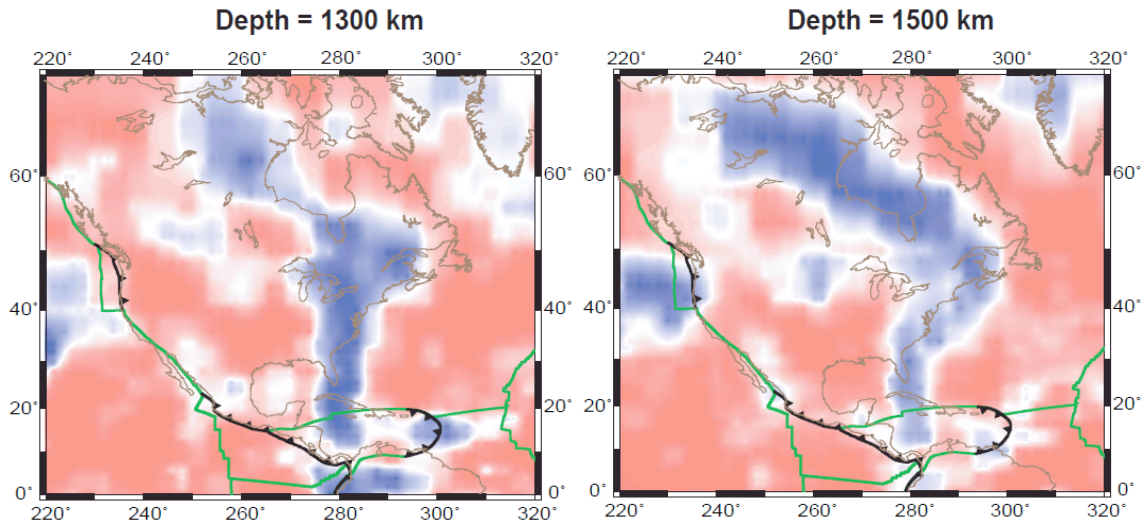
Figure 28 Map view at two different depths showing present-day Farallon remnant slabs in the lower mantle. Green lines represent spreading centers or transform faults, black tooth-line subduction zones, and dark brown, coastlines. Color scale is the same as that in Figure 26.

Since the restored flat-slab is a natural consequence of inverting the seismic image, more evidence, unrelated to seismic tomography, must be sought in order understand the physical mechanism causing the flat Farallon subduction. One possibility seems to be that the flat slab was created by usage of the stress guide implemented in the model. However, although the stress guide enhances the asymmetry of subduction, it does not explain the localized flat slab formation because the stress guide is uniformly, rather than locally, defined under the entire western North America. We will return to this issue in the next chapter.
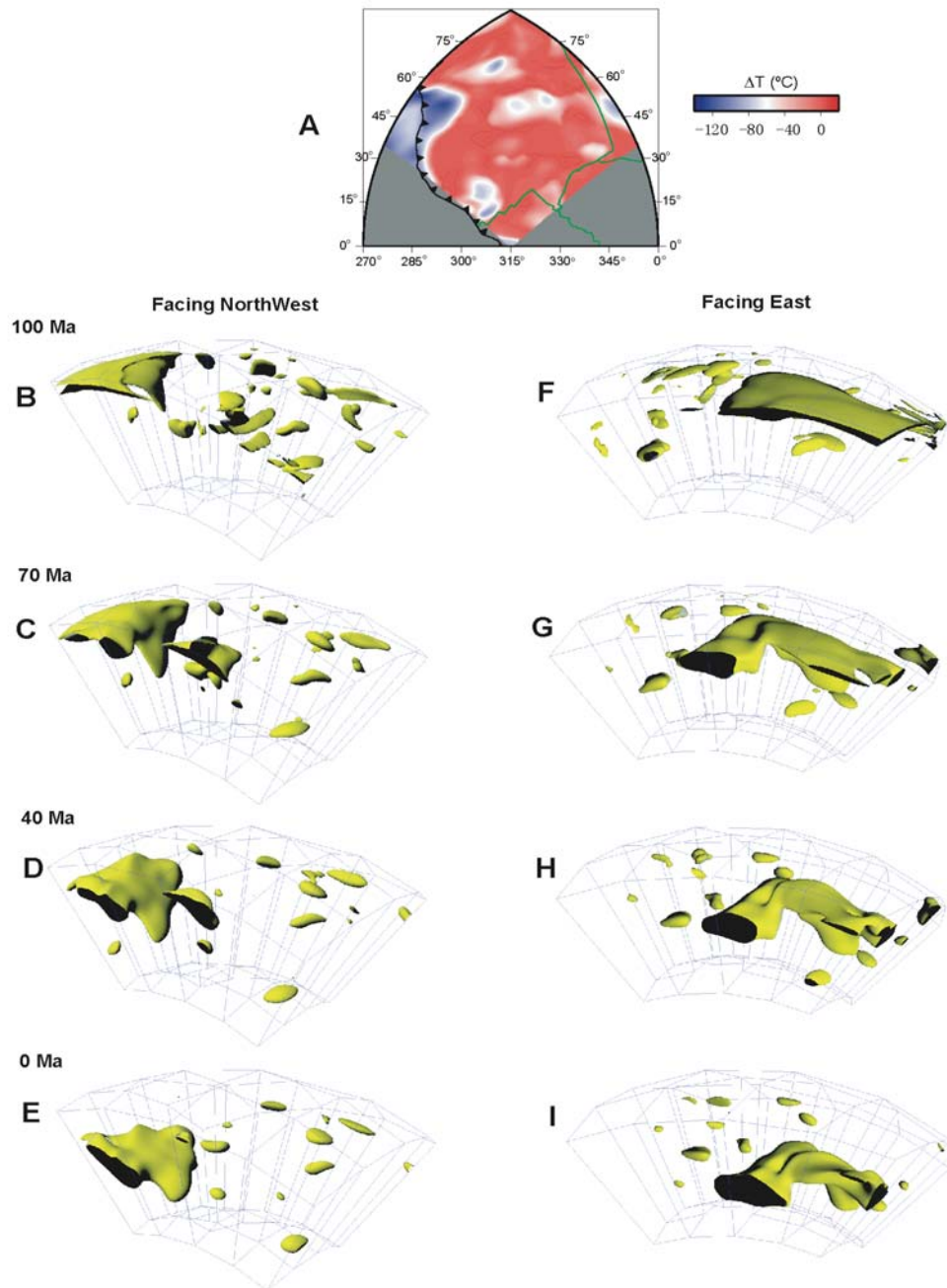
Figure 29 Three-dimensional view of the evolving Farallon slab in our preferred model, shown with isosurface of temperature field at 60 ºC lower than ambient mantle. This is a cut-out from a whole spherical shell (i.e., a Cap from *CitcomS* [Tan *et al.*, 2009]), where the top represents the surface and bottom the core-mantle boundary. The dynamics within the entire spherical domain was solved (12

caps), but only one cap is visualized here for clarity. The geographic location of the surface at 100 Ma is shown in A (the rectangular colored area), where the background temperature is at 223 km depth. The slab is viewed from two different angles, one facing the northwest (B−E) and the other toward the east (F−I), and four geological time periods are chosen from the initial time to the present day. The shaded green-yellow color represents the isosurface and dark area shows cross-sections of the slab against the edges of the cap.

Another possible reason for causing an isolated or segmented slab is the emergence of a spreading-center within the subducting plate. One candidate is the Kula-Farallon spreading ridge that formed during the Late Cretaceous time [Engebretson *et al*., 1986], which may have caused the northward translation of 'suspect' terranes along the western continental margin of North America [Debiche *et al*., 1987]. In fact, the plate motions we have used in driving the surface velocities of the inverse model include this phase of Farallon plate splitting [Fig. 25; Müller *et al*., 2008], but the splitting occurs later than the onset of flat slab subduction.